Supplementary Online Material (SOM):

Comparative anatomy of the carotid canal in the Miocene small-bodied catarrhine *Pliobates cataloniae*

Florian Bouchet [a, *], Alessandro Urciuoli [a], Amélie Beaudet [b, c, d, a], Marta Pina [e, a], Salvador Moyà-Solà [a, f, g], David M. Alba [a, *]

[a] *Institut Català de Paleontologia Miquel Crusafont, Universitat Autònoma de Barcelona, Edifici ICTA-ICP, c/ Columnes s/n, Campus de la UAB, 08193 Cerdanyola del Vallès, Barcelona, Spain*

[b] *Department of Archaeology, University of Cambridge, The Old Schools, Trinity Lane, Cambridge CB2 1TN, UK*

[c] *School of Geography, Archaeology and Environmental Studies, University of the Witwatersrand, 1 Jan Smuts Avenue, Braamfontein 2000, Johannesburg, South Africa*

[d] *Department of Anatomy, University of Pretoria, Lynnwood Road, Hatfield 0002, Pretoria, South Africa*

[e] *Department of Earth and Environmental Sciences, University of Manchester, Williamson Building, Oxford Road, Manchester M13 9PL, UK*

[f] *Institució Catalana de Recerca i Estudis Avançats (ICREA), Passeig de Lluís Companys 23, 08010 Barcelona, Spain*

[g] *Unitat d'Antropologia (Dept. BABVE), Universitat Autònoma de Barcelona, Edifici C, Facultat de Biociències, Campus de la UAB, 08193 Cerdanyola del Vallès, Barcelona, Spain*

[*] Corresponding authors.

E-mail addresses: florian.bouchet@icp.cat (F. Bouchet); david.alba@icp.cat (D.M. Alba).

SOM S1

Extended methodology

3D carotid canal surfaces

For each specimen, the carotid canal was virtually extracted through semiautomatic threshold-based segmentation in Avizo v. 7.0 (Visualization Sciences Group, Bordeaux). The right carotid canal was segmented for most specimens; when this was not possible, the left canal was segmented and mirrored. We devised a protocol to identify the two ends (anterior and posterior) of the carotid canal and cut them at homologous points (Fig. 1; SOM Fig. S1), to obtain 3D canal surfaces comparable among specimens. For the posterior end of the canal, we placed landmarks on its external aperture (carotid foramen; SOM Fig. S1a, b), computed the best-fit plane to these landmarks, translated it to be located at the centroid of the landmark set, and finally cut the canal (Fig. 1a). The centroid of the landmarks on the carotid foramen was taken as the posterior endpoint of the canal (Fig. 1l).

The methodology employed to cut the anterior part of the carotid canal was more complex, because its opening on the endocranial surface of the petrosal is irregular and displays a variable outline among individuals. Furthermore, it was not completely preserved in fossil specimens we included here. We started by defining a landmark located posteriorly to the canal opening, and used it to determine the anterior limit at which we could later cut the anterior part of the canal. We defined a landmark termed 'intersection ridge–groove' (IRG) that corresponds to the intersection between the anterior pyramidal ridge and the groove of the greater superficial petrosal nerve (SOM Fig. S1c, d; Table 2). Based on IRG, we applied a semiautomatic protocol coded on R v. 3.6.3 (R Core Team, 2020; see script in SOM File S1) to find the plane orthogonal to the 3D carotid canal surface passing through IRG. In particular, the 3D canal surface is first generated and smoothed in Avizo (using a constrained smoothing and a smoothing extent of 3) and then imported as a cloud of points in R (Fig. 1b); the orthogonal projection of IRG onto the canal (IRG') is calculated (Fig. 1c). These two points (IRG and IRG') define a main axis, around which infinity of points can be generated, further enabling the creation of infinity of planes. Indeed, a plane can be defined by three points expressed as two vectors, and the axis defined by IRG and IRG' corresponds to one of the two vectors necessary to compute the orthogonal plane to the canal (passing through IRG), because IRG' is the orthogonal projection of IRG onto the canal. However, to obtain the second vector, a third point is required, which cannot be defined a priori. We decided to

define the cutting plane as the one that is orthogonal to the 3D canal surface (and therefore to the canal streamline) and thus that minimizes the cross-sectional area resulting from the cut. The protocol generates multiple cutting planes—defined on IRG, IRG', and multiple possible third points—and calculates the cut area for each of them. In particular, we created 360 equally distributed points (differing in 1° of orientation) around the IRG–IRG' axis (Fig. 1d) and computed the cutting cross-sectional area for all the 360 possible cutting planes (Fig. 1e, f). For each plane possibility, among the cloud of points representing the canal, the points that are closest to the plane (i.e., those having an orthogonal distance to the plane equal or shorter than the distance between two adjacent points of the cloud) are identified (Fig. 1g). Among them, only the most external ones are kept and used to form a convex hull approximating the contour of the canal cross-section (Fig. 1h). The area subtended by the convex hull is then subdivided in *n*-2 triangles, where *n* is the number of points that form the hull, using one of the points as the shared vertex (the most acute one) for all the triangles; the area of the triangles is computed and their sum is used as an approximation of the total area of the cross-section (Fig. 1i). The plane for which the resulting cross-sectional area is the smallest is kept and used as reference for cutting the canal at its anterior end (Fig. 1i, j). The centroid of the cross-section obtained by cutting with this orthogonal plane (Fig. 2h–i) is calculated and used as the anterior endpoint of the canal (Fig. 1l).

Carotid canal orientation

We quantified the orientation of the carotid canal within the petrosal by computing a 3D vector representing the canal direction and decomposing it into two 2D angles relative to standard anatomical planes: one angle represents the canal superior orientation (2DYZA) along the (para)sagittal plane, and the other represents its medial orientation (2DXYA) along a transverse plane—respectively corresponding to canal 'orientation' and 'direction' sensu Alba et al. (2015: Tables S5 and S6). The 3D vector representing the canal was computed as a single direction, from the posterior to the anterior endpoints of the canal. All the specimens were first put in the same coordinate system by performing a generalized Procrustes analysis (GPA; Rohlf and Slice, 1990; Bookstein, 1991) using the R package 'Geomorph' v. 3.3.1 (Adams et al., 2019) based on nine petrosal/tympanic landmarks (Fig. 2; Table 2). This allowed us to scale, orient, and locate the petrosals in a standardized way within a common Cartesian coordinate system. The translation-scaling-rotation parameters resulting from this

alignment were then extracted and applied to the two endpoints of the canal vector. Performing the alignment on the petrosal, instead of the canal endpoints or both structures simultaneously, enables the retention of the canal position, orientation and shape inside the petrosal, for each specimen. The coordinates of the posterior and anterior endpoints after the petrosal/tympanic-based alignment were used to compute the 3D vector representing the 3D canal direction.

As the specimens were prealigned, we were able to use a single reference vector to calculate the two 2D angles. Despite some variation among the sample, there is an overall correspondence (with no extreme deviations) between spatial axes of the common Cartesian coordinate system and canal directions after alignment: the X-axis corresponds to the anteromedial–posterolateral direction of the canal, the Y-axis corresponds to its inferomedial–superolateral direction, and the Z-axis corresponds to its anterolateral–posteromedial direction. Considering these correspondences, 2DYZA was calculated as the 2D angle between the YZ coordinates of the canal vector and a reference vector with coordinates (1, -1) corresponding to the cranial anteroposterior axis (from posterior to anterior). In turn, 2DXYA was calculated as the 2D angle between the XY coordinates of the canal vector and a reference vector with coordinates (-0.2, 1) also corresponding to the cranial anteroposterior axis (from posterior to anterior). While in anthropoids the canal runs from a posterolateral location to an anteromedial location, after alignment some specimens display a canal running almost anteroposteriorly or slightly (postero)medio(antero)laterally. To take into account those exceptions the 2DXYA angle was calculated so that positive values correspond to medially oriented canals and negative values identify canals (only a few) slightly laterally oriented.

Because the alignment is based on petrosal/tympanic landmarks, one should consider the possibility that two specimens possessing similar angles relative to the petrosal may display different angles if computed relative to the whole cranium, depending on the orientation and position of the petrosal inside the cranium. However, based on Spoor's (1993) data, differences of superior petrosal surface orientations in the sagittal plane and superior and inferior petrosal surface orientations in the transverse plane are not significant among the main crown anthropoid clades. Furthermore, relying on petrosal/tympanic landmarks for scaling-translating-orienting carotid canal specimens, instead of landmarks from the cranium as a whole, has several advantages besides enabling the analysis of fragmentary fossil

remains. In particular, this procedure may prevent alignment problems related to striking shape differences between extant lineages (such as the elongated muzzle of some papionins, the much more globulous neurocranium of some hominoids, the longer parietal of platyrrhines, etc.), because the variation in petrosal shape seems less marked.

Carotid canal proportions

After cutting the two ends of the carotid canal, the 3D canal surfaces were generated again without smoothing in Avizo, and the volume (V, in mm^3) of the closed 3D surfaces was computed using the module 'Surface Area Volume'. The 3D surfaces were then reimported in R and, for each specimen, we calculated canal length (L, in mm). To do so, we computed nine semilandmarks corresponding to the centroids of the canal cross-sections obtained by means of nine equidistant slices generated along the two canal endpoints (i.e., type III landmarks; Bookstein, 1991). The resulting 11 streampoints (2 endpoints + 9 centroids in between) were used to generate 8 equidistant streampoints between the 2 endpoints using the 'digit.curve' function of 'Geomorph' v. 3.3.1—the sliding process embedded in this function requiring to set a number of final points smaller than the original number of points. Based on these 10 equidistant streampoints representing the canal streamline we computed nine segments (distances), whose sum was taken as canal length.

Carotid canal course within the petrosal

To assess the course of the carotid canal within the petrosal we used a similar approach to that employed for computing L. We took the 10 equidistant streampoints previously computed during the calculation of L. As mentioned above, these 10 streampoints follow the streamline of the canal, i.e., de facto they represent the canal course. Then we applied the translation-scaling-rotation parameters resulting from the alignment of the petrosals described above to the 10 streampoints. As for the canal orientation, this procedure allowed us retaining the information on the variation of position, orientation and shape of the canal inside the petrosal. The configuration of the 10 canal streampoints obtained after alignment therefore represents the course of the carotid canal within the petrosal.

Phylogenetic tree

To compute PGLS regressions and quantify phylogenetic signal we used a time-calibrated tree representing the phylogenetic relationships among the extant taxa included in the comparative sample. The tree was derived from the 10kTrees website (Arnold et al., 2010), with some modifications to account for not included species in the 10kTrees website: (1) *Simias concolor* was added as the sister taxon of *Nasalis larvatus* with a divergence time at 2.16 Ma (Springer et al., 2012); (2) *Presbytis rubicunda* was replaced by data on *Presbytis melalophos*, which is its closest species (Meyer et al., 2011; Springer et al., 2012); (3) *Pithecia monachus* was added as the sister taxon of *Pithecia pithecia*, with a divergence time between both taxa set at 3.46 Ma (Springer et al., 2012); (4) *Chiropotes chiropotes* was added as the sister taxon of *Pithecia* spp., with a divergence time set at 13.27 Ma (Springer et al., 2012); (5) *Plecturocebus cupreus* was added as the sister taxon of the *Chiropotes-Pithecia* clade, with a divergence time set at 19.84 Ma (Springer et al., 2012).

We further used two different hypotheses for the phylogenetic relationships among the investigated fossil genera and extant catarrhines, with the exception of *Victoriapithecus*, considered a stem cercopithecoid in both instances. The tips of the fossil taxa were set based on their geological age: *Victoriapithecus* at 15 Ma (Benefit, 1999); *Epipliopithecus* at 14.15 Ma (as estimated from the midpoint of MN6 in Europe based on van der Meulen et al., 2011); *Pliobates* at 11.62 Ma (Alba et al. 2017); and *Ekembo* at 17.8 Ma (as the midpoint of the maximum-minimum range of the Kulu Formation in Rusinga Island, where *E. heseloni* has been found; Drake et al., 1988; Peppe et al., 2009; Harrison, 2010). The divergence between *Victoriapithecus* and crown cercopithecoids was set 1 Myr older than the cercopithecine-colobine divergence (21.41 Ma). Under hypothesis 1 (SOM Fig. S2a), *Epipliopithecus, Ekembo*, and *Pliobates* are considered successive stem hominoids, following the results of Alba et al.'s (2015) cladistic analysis. Their divergence from crown hominoids was set 3, 2 and 1 Myr before the hominid-hylobatid divergence date (19.61 Ma), respectively. In contrast, under hypothesis 2 (SOM Fig. S2b) only *Ekembo* is considered a stem hominoid, while both *Pliobates* and *Epipliopithecus* are considered stem catarrhines within a pliopithecoid clade, following the results of other cladistic analyses (Nengo et al., 2017; Gilbert et al., 2020). The divergence between *Epipliopithecus* and *Pliobates* was set 1 Myr older than the oldest occurrence of either of them (1 Myr older than *Epipliopithecus*, i.e., 15.15 Ma), while the divergence between pliopithecoids and crown catarrhines was set 1 Myr older than the divergence between cercopithecoids and hominoids (30 Ma), as this is

older than the oldest documented occurrence of pliopithecoids in the fossil record (18–17 Ma; Harrison, 2013, 2017; Begun, 2017).

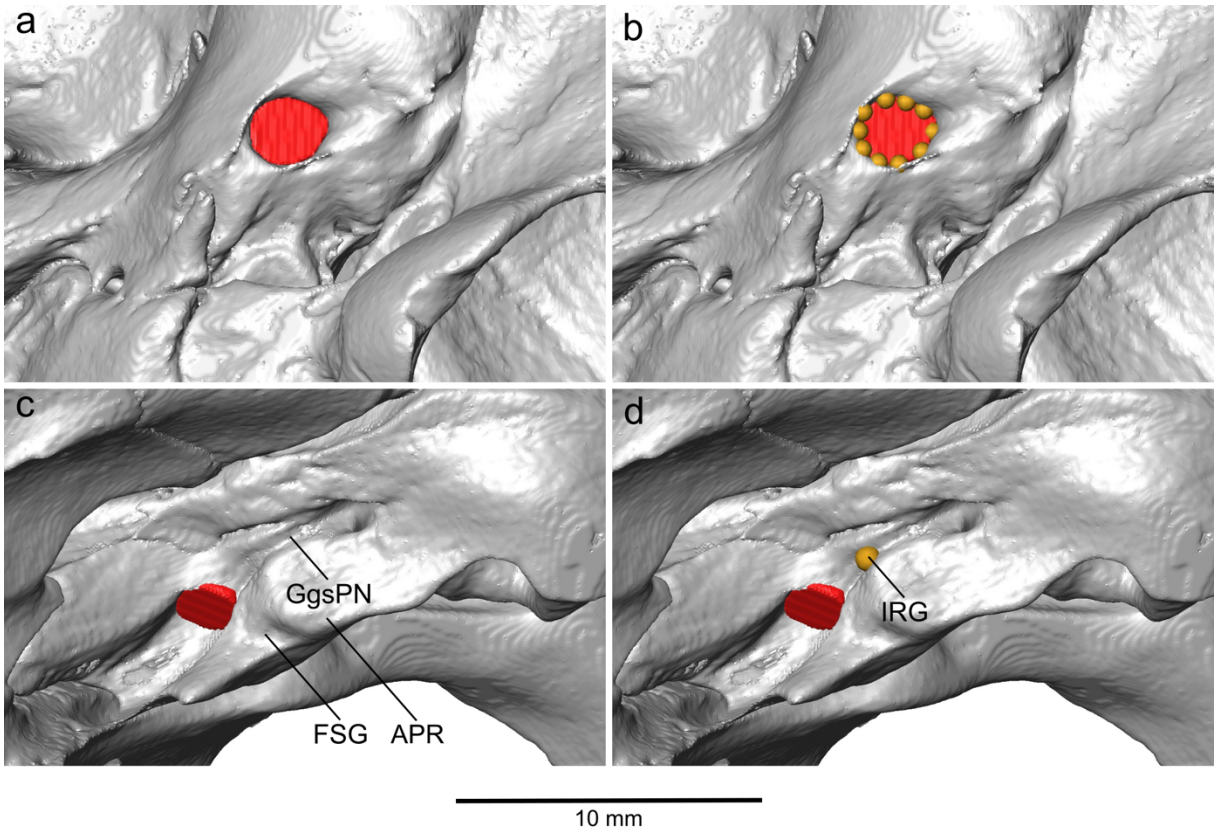

SOM Figure S1. Landmarks used for delimiting the extremities of the carotid canal as exemplified in a *Macaca fascicularis* individual. The 3D canal surface (in red; a) is posteriorly defined by putting landmarks on the rim of the carotid foramen (b). The anterior limit of the canal (in red; c) is identified by placing a landmark (IRG) at the intersection between the anterior pyramidal ridge and the groove for the greater superficial petrosal nerve (d). Abbreviations: APR = anterior pyramidal ridge; FSG = fossa for the semilunar ganglion; GgsPn = groove of the greater superficial petrosal nerve; IRG = intersection ridge–groove.

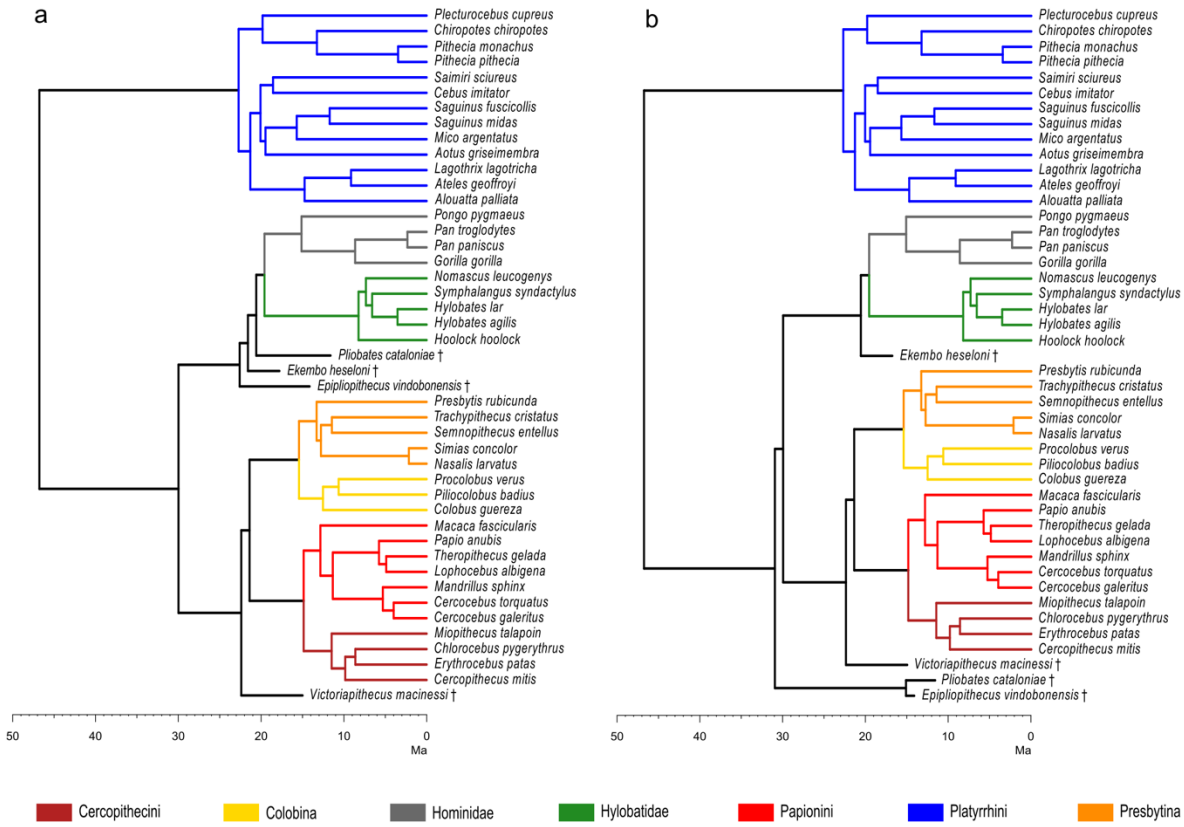

SOM Figure S2. Time-calibrated phylogenetic trees of extant anthropoids and selected extinct catarrhines (denoted by a dagger) used in this paper to compute phylogenetic generalized least-squares regressions (excluding fossils), phylogenetic signal (excluding fossils), and phylomorphospaces. The trees are based on molecular data and derived from the 10kTrees website v. 3 (Arnold et al., 2010) with some modifications based on Meyer et al. (2011) and Springer et al. (2012). Extinct taxa were added a posteriori according to the two phylogenetic hypotheses considered in this paper: a) *Epipliopithecus*, *Ekembo* and *Pliobates* are considered successive stem hominoids following Alba et al. (2015: Fig. 8); b) *Epipliopithecus* and *Pliobates* are considered sister taxa within a stem catarrhine pliopithecoid clade and *Ekembo* is considered a stem hominoid, following Nengo et al. (2017: Fig. 5) and Gilbert et al. (2020: Fig. 4). *Victoriapithecus* is considered a stem cercopithecoid under both hypotheses. The point estimates for extinct taxa correspond to their occurrence in the fossil record (Drake et al., 1988; Benefit, 1999; Peppe et al., 2009; van der Meulen et al., 2011; Alba et al., 2017). See SOM S1 for further details.

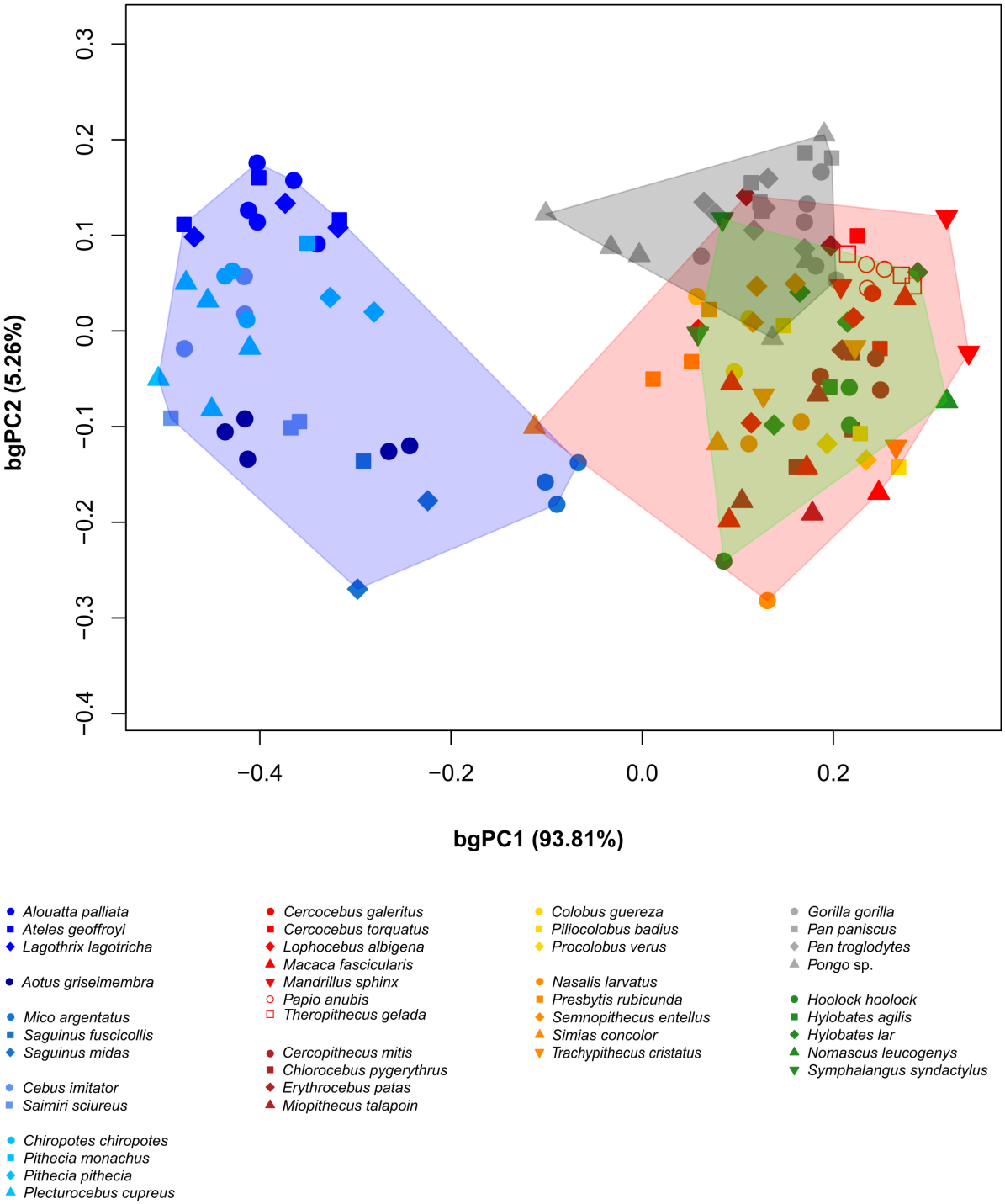

SOM Figure S3. Results of the cross-validated between-group principal component analysis (CV-bgPCA) using main extant anthropoid clades as the grouping factor, as depicted by a bivariate plot of bgPC2 vs. bgPC1. Convex hulls correspond to: platyrrhines (blue), cercopithecids (red), hylobatids (green), and hominids (gray). Abbreviation: CV-bgPC = cross-validated between-group principal component.

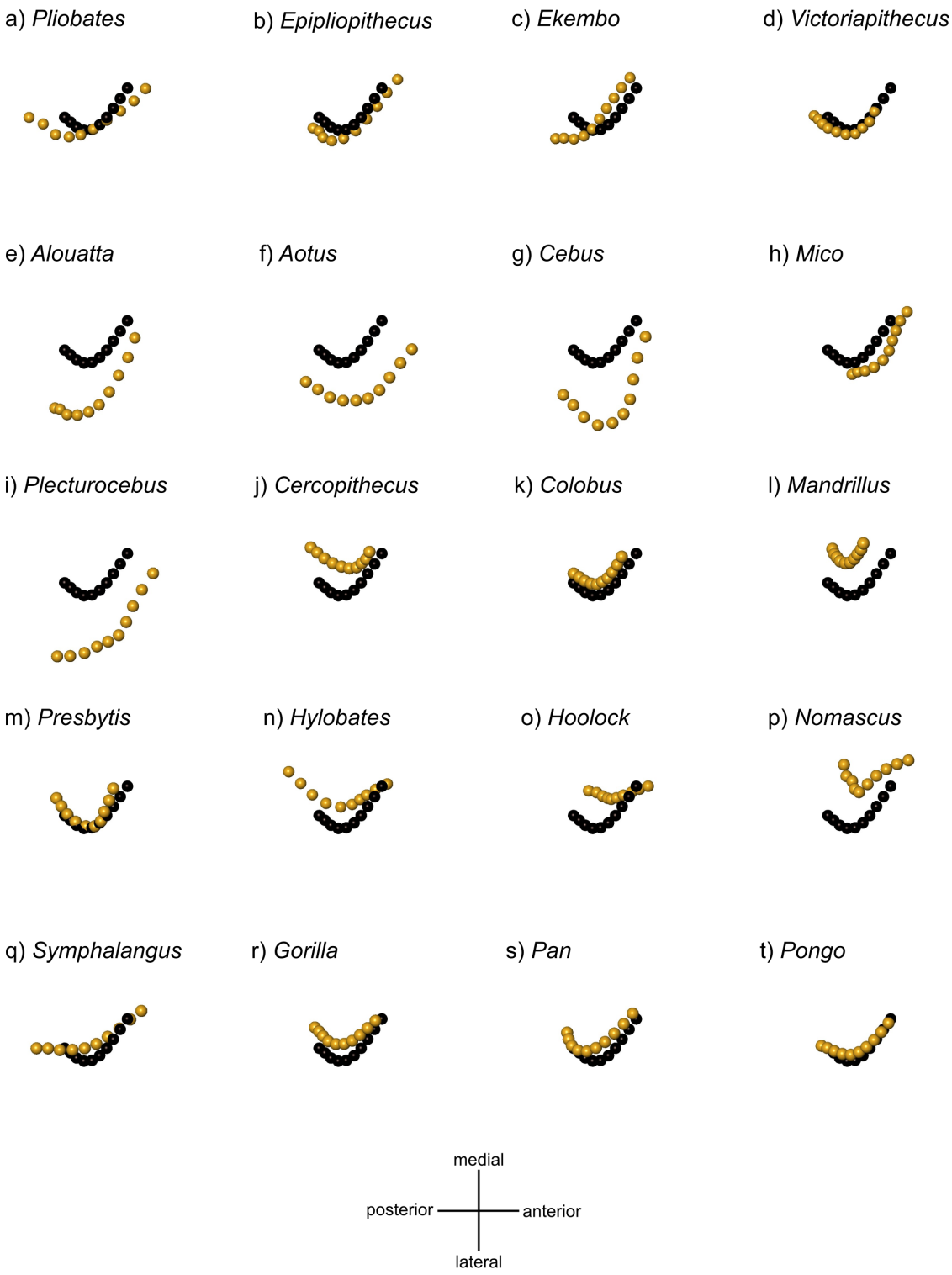

SOM Figure S4. Configurations of the carotid canal course in *Pliobates* compared with fossil and extant anthropoids in superior view: a) *Pliobates* (IPS58443.1); b) *Epipliopithecus* (NHMW 1970/1397/0003); c) *Ekembo* (KNM-RU 2036al); d) *Victoriapithecus* (KNM-MB 29100); e) *Alouatta*; f) *Aotus*; g) *Cebus*; h) *Mico*; i) *Plecturocebus*; j) *Cercopithecus*; k) *Colobus*; l) *Mandrillus*; m) *Presbytis*; n) *Hylobates*; o) *Hoolock*; p) *Nomascus*; q)

Symphalangus; r) *Gorilla*; s) *Pan*; t) *Pongo*. The mean configuration computed for the whole anthropoid sample is represented by black dots while configurations for specimens are represented in beige. For a better understanding of the canal course variation in space the anthropoid mean configuration was used as a reference for visualizing all the configurations at the same relative scale.

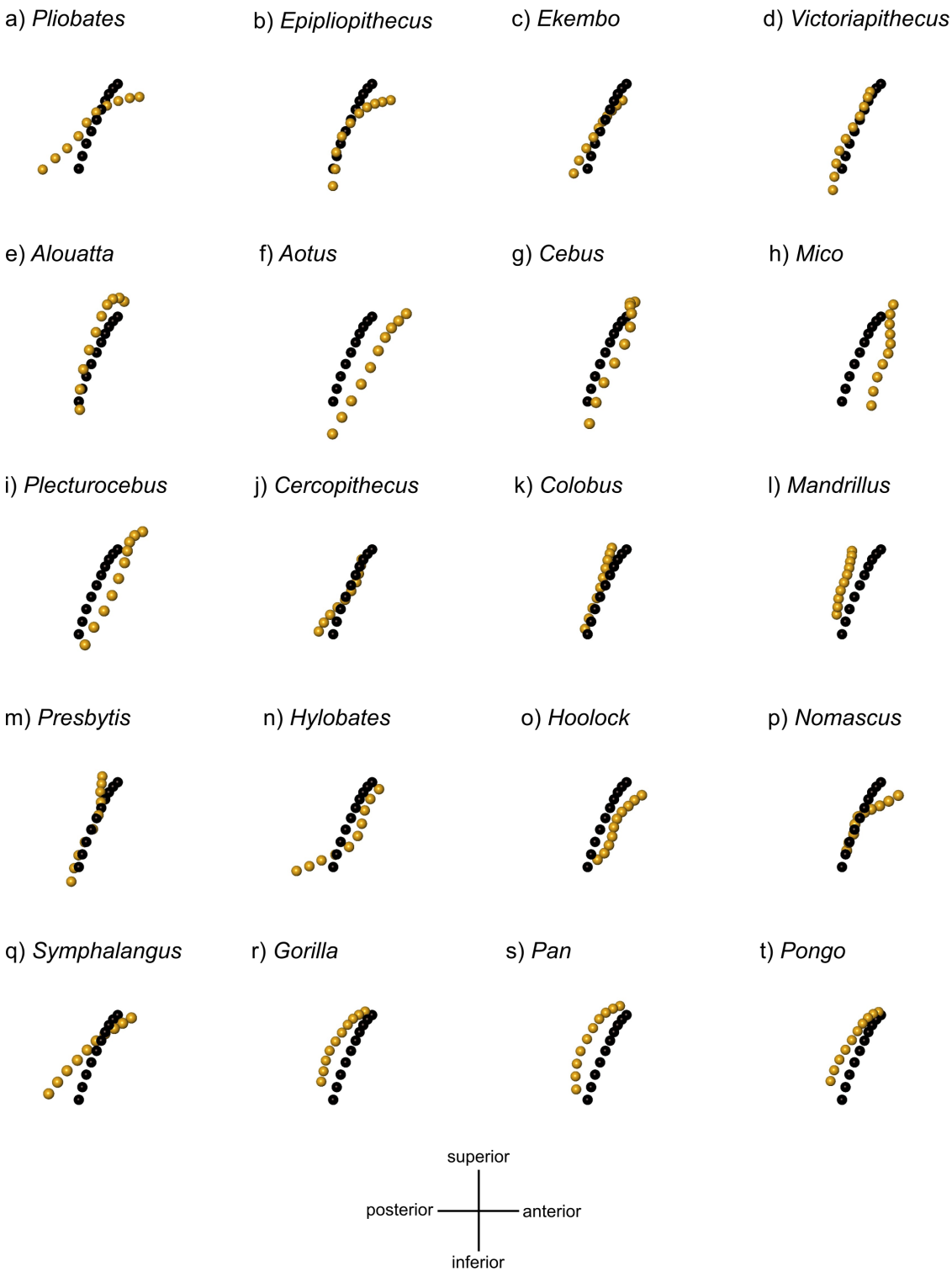

SOM Figure S5. Configurations of the carotid canal course in *Pliobates* compared with fossil and extant anthropoids in lateral view: a) *Pliobates* (IPS58443.1); b) *Epipliopithecus* (NHMW 1970/1397/0003); c) *Ekembo* (KNM-RU 2036al); d) *Victoriapithecus* (KNM-MB 29100); e) *Alouatta*; f) *Aotus*; g) *Cebus*; h) *Mico*; i) *Plecturocebus*; j) *Cercopithecus*; k) *Colobus*; l) *Mandrillus*; m) *Presbytis*; n) *Hylobates*; o) *Hoolock*; p) *Nomascus*; q) *Symphalangus*; r) *Gorilla*;

s) *Pan*; t) *Pongo*. The mean configuration computed for the whole anthropoid sample is represented by black dots while configurations for specimens are represented in beige. For a better understanding of the canal course variation in space the anthropoid mean configuration was used as a reference for visualizing all the configurations at the same relative scale.

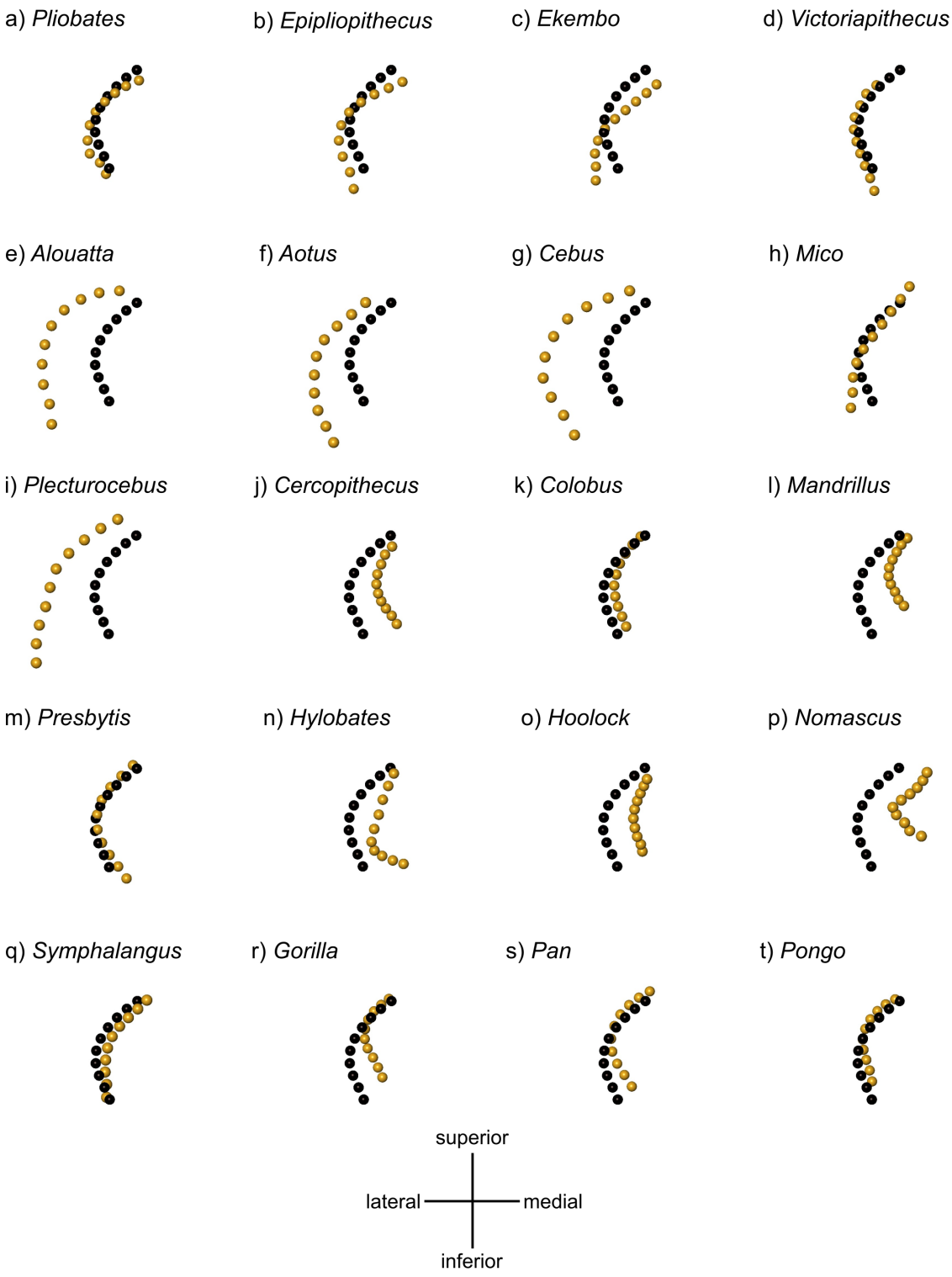

SOM Figure S6. Configurations of the carotid canal course in *Pliobates* compared with fossil and extant anthropoids in anterior view: a) *Pliobates* (IPS58443.1); b) *Epipliopithecus* (NHMW 1970/1397/0003); c) *Ekembo* (KNM-RU 2036al); d) *Victoriapithecus* (KNM-MB 29100); e) *Alouatta*; f) *Aotus*; g) *Cebus*; h) *Mico*; i) *Plecturocebus*; j) *Cercopithecus*; k) *Colobus*; l) *Mandrillus*; m) *Presbytis*; n) *Hylobates*; o) *Hoolock*; p) *Nomascus*; q)

Symphalangus; r) *Gorilla*; s) *Pan*; t) *Pongo*. The mean configuration computed for the whole anthropoid sample is represented by black dots while configurations for specimens are represented in beige. For a better understanding of the canal course variation in space the anthropoid mean configuration was used as a reference for visualizing all the configurations at the same relative scale.

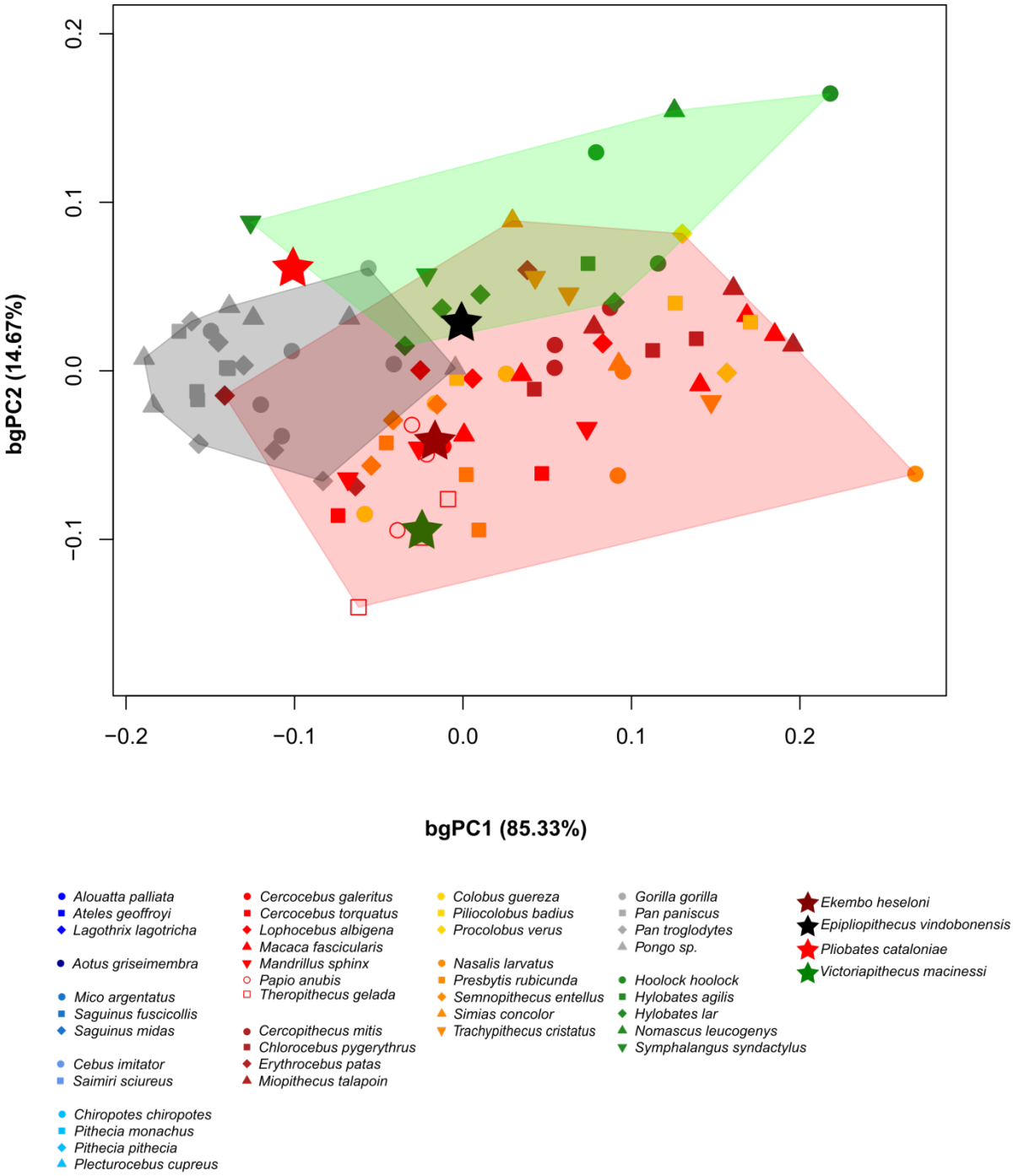

SOM Figure S7. Results of the between-group principal component analysis (bgPCA) based on carotid canal course variation among the catarrhine subsample, as depicted by a bivariate plot of bgPC2 vs. bgPC1. Convex hulls correspond to: cercopithecids (red), hylobatids (green), and hominids (gray). Abbreviation: bgPC = between-group principal component.

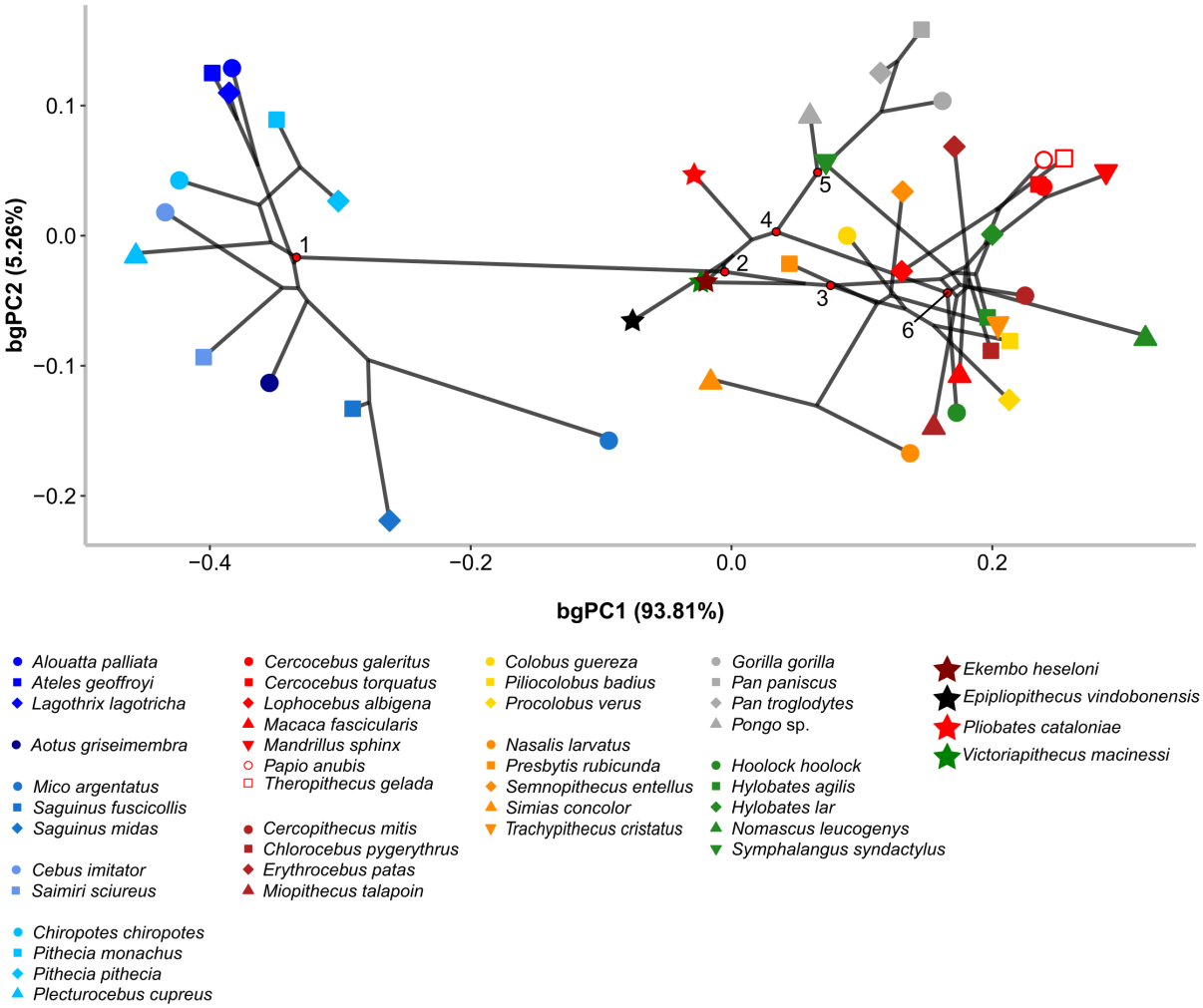

SOM Figure S8. Phylomorphospace of carotid canal course variation in extant anthropoids and extinct Miocene catarrhines including *Pliobates*. *Epipliopithecus*, *Ekembo* and *Pliobates* are considered successive stem hominoids following Alba et al. (2015: Fig. 8), while *Victoriapithecus* is considered a stem cercopithecoid. See SOM Figure S2a for a representation of this phylogenetic hypothesis. Ancestral nodes: 1 = crown platyrrhines; 2 = crown catarrhines; 3 = crown cercopithecoids; 4 = crown hominoids; 5 = crown hominids; 6, crown hylobatids.

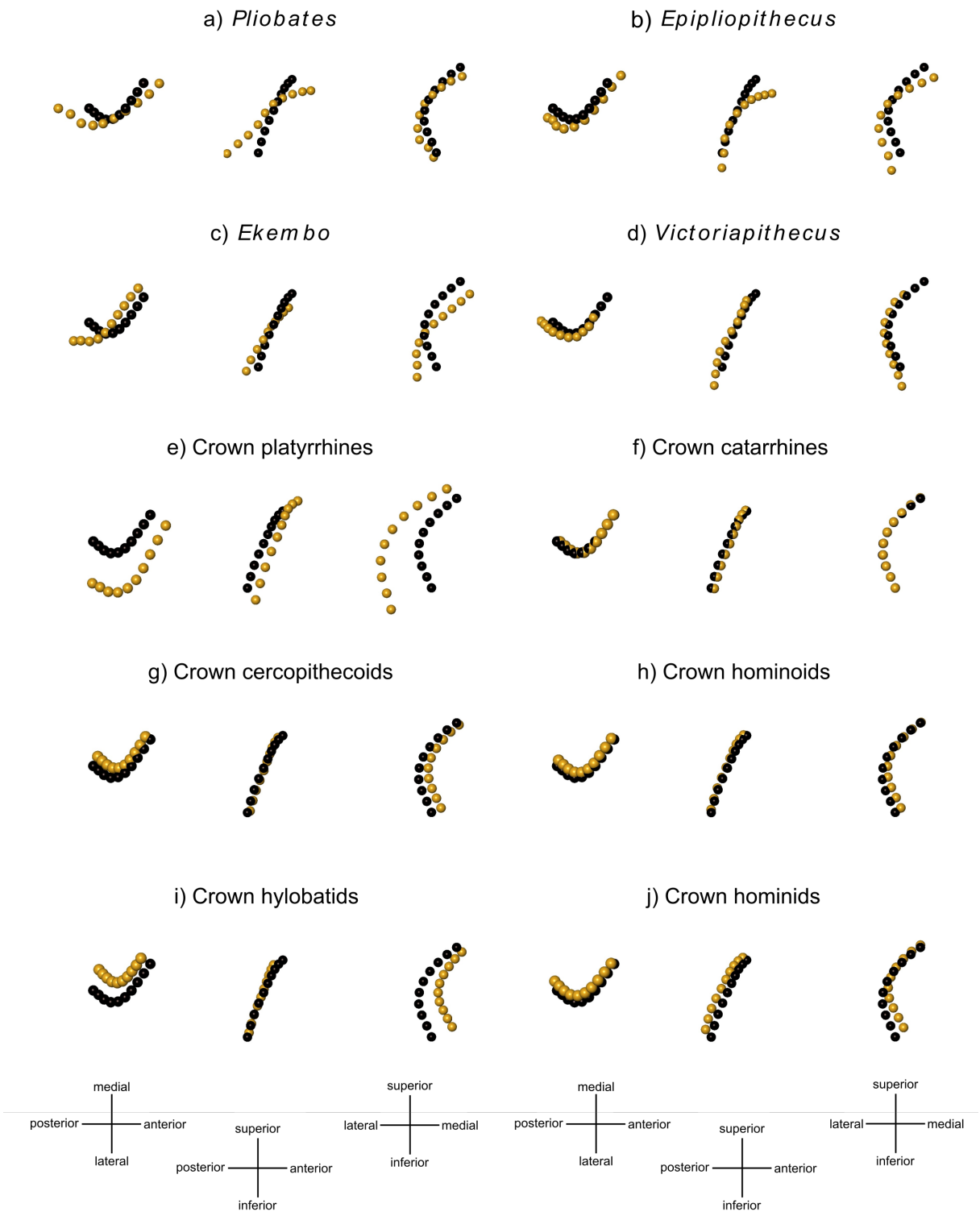

SOM Figure S9. Configurations of the carotid canal course in *Pliobates* compared with other Miocene catarrhines and with the reconstructed carotid canal course for the last common ancestors (LCAs) of various anthropoid clades: a) *Pliobates* (IPS58443.1); b) *Epipliopithecus* (NHMW 1970/1397/0003); c) *Ekembo* (KNM-RU 2036al); d) *Victoriapithecus* (KNM-MB 29100); e) crown platyrrhines; f) crown catarrhines; g) crown cercopithecoids; h) crown

hominoids; i) crown hylobatids; j) crown hominids. The canal courses of the LCAs have been inferred based on the phylomorphospace displayed in SOM Figure S8. For each specimen/LCA, the configurations are displayed in superior (left), lateral (middle), and anterior (right) views. The mean configuration computed for the whole anthropoid sample is represented by black dots, while configurations for Miocene catarrhines and LCAs are represented in beige. The anthropoid mean configuration was used as a reference for visualizing all the configurations at the same relative scale.

SOM Table S1

List of extant anthropoid specimens included in this work. µCT scans were mainly downloaded from MorphoSource (https://www.morphosource.org, Duke University) or provided by Sergio Almécija (used in Urciuoli et al., 2020; µCT scans stored at the AMNH, New York, USA) and the Institut Català de Paleontologia Miquel Crusafont (ICP; Sabadell, Spain).

Species	ID	Source	Voxel size (mm)	Sex	DOI/Ark identifier/Occurrence ID	MorphoSource ID
Alouatta palliata	DUEALP 04	Morphosource	0.061	M	—	S1924
Alouatta palliata	DUEALP 06	Morphosource	0.067	M	—	S78
Alouatta palliata	DUEALP 13	Morphosource	0.052	F	—	S1108
Alouatta palliata	DUEALP 14	Morphosource	0.055	F	—	S1925
Alouatta palliata	DUEALP 16	Morphosource	0.058	F	—	S80
Aotus griseimembra	USNM 281551	Morphosource	0.036	M	http://n2t.net/ark:/65665/31db1d5a6-9879-459b-b08e-89e55015542e	S3994
Aotus griseimembra	USNM 281552	Morphosource	0.034	F	http://n2t.net/ark:/65665/3b29a3a53-e84f-4f04-9e48-bc203f45765c	S3980
Aotus griseimembra	USNM 284776	Morphosource	0.035	F	http://n2t.net/ark:/65665/34fb1e7f4-ed5d-4d36-9f36-e7741dcd02bd	S3996
Aotus griseimembra	USNM 284777	Morphosource	0.035	M	http://n2t.net/ark:/65665/30fe89705-6148-4207-9b9c-f5435c669587	S3997
Aotus griseimembra	USNM 284779	Morphosource	0.038	F	http://n2t.net/ark:/65665/354427a46-c645-4785-90d2-b08310d3110d	S3979
Ateles geoffroyi	AMNH-M 26593	Morphosource	0.062	F	urn:catalog:AMNH:Mammals:M-26593	S5312
Ateles geoffroyi	MCZ 10138	Morphosource	0.063	F	http://dx.doi.org/10.17602/M2/M2917	S971
Ateles geoffroyi	MCZ 29628	Morphosource	0.063	F	http://dx.doi.org/10.17602/M2/M2919	S973
Cebus imitator	MCZ 10135	Morphosource	0.080	F	http://dx.doi.org/10.17602/M2/M5151	S1676
Cebus imitator	MCZ 34326	Morphosource	0.080	F	http://dx.doi.org/10.17602/M2/M5148	S1673
Cebus imitator	MCZ 34353	Morphosource	0.080	F	http://dx.doi.org/10.17602/M2/M5147	S1672
Cercocebus galeritus	AMNH-M 52641	Morphosource	0.068	M	urn:catalog:AMNH:Mammals:M-52641	S1513
Cercocebus torquatus	AMNH-M 70063	Morphosource	0.118	M	urn:catalog:AMNH:Mammals:M-70063	S4046
Cercocebus torquatus	MCZ 32625	Morphosource	0.091	M	http://dx.doi.org/10.17602/M2/M2589	S777
Cercopithecus mitis	MCZ 25022	Morphosource	0.080	F	http://dx.doi.org/10.17602/M2/M2929	S983
Cercopithecus mitis	MCZ 26832	Morphosource	0.080	F	http://dx.doi.org/10.17602/M2/M2930	S984

Cercopithecus mitis	MCZ 7088	Morphosource	0.080	F	http://dx.doi.org/10.17602/M2/M2927	S981
Chiropotes chiropotes	USNM 388161	Morphosource	0.047	F	http://n2t.net/ark:/65665/3bd51f984-2926-4bd6-a368-1c2be2fb4a87	S3926
Chiropotes chiropotes	USNM 388163	Morphosource	0.047	F	http://n2t.net/ark:/65665/3007743ab-5f8c-4542-a384-bc68d16bd910	S3928
Chiropotes chiropotes	USNM 388165	Morphosource	0.049	M	http://n2t.net/ark:/65665/3b5260e90-e411-4638-9257-f4e65440a1ea	S3935
Chlorocebus pygerythrus	SIU 4799	Morphosource	0.050	F	—	S4045
Chlorocebus pygerythrus	SIU 4800	Morphosource	0.046	F	—	S4047
Chlorocebus pygerythrus	SIU 4801	Morphosource	0.055	M	—	S4048
Colobus guereza	AMNH-M 52211	Morphosource	0.073	M	urn:catalog:AMNH:Mammals:M-52211	S1143
Colobus guereza	AMNH-M 52213	Morphosource	0.066	F	urn:catalog:AMNH:Mammals:M-52213	S3768
Colobus guereza	AMNH-M 52238	Morphosource	0.068	F	urn:catalog:AMNH:Mammals:M-52238	S1215
Erythrocebus patas	MCZ 47015	Morphosource	0.083	M	http://dx.doi.org/10.17602/M2/M2923	S977
Erythrocebus patas	MCZ 47016	Morphosource	0.083	M	http://dx.doi.org/10.17602/M2/M2924	S978
Erythrocebus patas	MCZ 47018	Morphosource	0.083	F	http://dx.doi.org/10.17602/M2/M2926	S980
Gorilla gorilla	AMNH-A 999686	Morphosource	0.131	M	—	S5189
Gorilla gorilla	AMNH-M 54356	Morphosource	0.106	F	urn:catalog:AMNH:Mammals:M-54356	S5125
Gorilla gorilla	MCZ 17684	Morphosource	0.126	F	http://dx.doi.org/10.17602/M2/M2943	S644
Gorilla gorilla	MCZ 26850	Morphosource	0.123	F	http://dx.doi.org/10.17602/M2/M2947	S995
Gorilla gorilla	MCZ 37264	Morphosource	0.126	F	http://dx.doi.org/10.17602/M2/M2949	S997
Gorilla gorilla	MCZ 46325	Morphosource	0.126	F	http://dx.doi.org/10.17602/M2/M2955	S1001
Hoolock hoolock	AMNH-M 112720	Morphosource	0.052	M	urn:catalog:AMNH:Mammals:M-112720	S1206
Hoolock hoolock	AMNH-M 201743	Morphosource	0.064	F	urn:catalog:AMNH:Mammals:M-201743	S12604
Hoolock hoolock	AMNH-M 83425	AMNH	0.084	F	urn:catalog:AMNH:Mammals:M-83425	S1209
Hylobates agilis	IPS3773	CENIEH	0.052	?	—	
Hylobates lar	MCZ 41412	Morphosource	0.067	F	http://dx.doi.org/10.17602/M2/M2961	S1005
Hylobates lar	MCZ 41418	Morphosource	0.067	F	http://dx.doi.org/10.17602/M2/M2967	S1008
Hylobates lar	MCZ 41421	Morphosource	0.067	F	http://dx.doi.org/10.17602/M2/M2969	S1009
Hylobates lar	MCZ 41424	Morphosource	0.067	F	http://dx.doi.org/10.17602/M2/M3007	S1017

Lagothrix lagotricha	USNM 269839	Morphosource	0.058	F	http://n2t.net/ark:/65665/3d05a410d-2384-4415-a7cb-9d53b2d58726	S3004
Lagothrix lagotricha	USNM 461930	Morphosource	0.060	F	http://n2t.net/ark:/65665/35d3a334f-9bc6-48e9-864d-6fe2cf11beba	S3006
Lagothrix lagotricha	USNM 545879	Morphosource	0.058	M	http://n2t.net/ark:/65665/30f0814b2-a584-4c20-96c2-fbcb4e5778e2	S283
Lophocebus albigena	MCZ 14725	Morphosource	0.090	F	http://dx.doi.org/10.17602/M2/M2626	S794
Lophocebus albigena	MCZ 18614	Morphosource	0.090	M	http://dx.doi.org/10.17602/M2/M2622	S790
Lophocebus albigena	MCZ 22737	Morphosource	0.090	F	http://dx.doi.org/10.17602/M2/M2621	S789
Macaca fascicularis	MCZ 12758	Morphosource	0.062	F	http://dx.doi.org/10.17602/M2/M3028	S1032
Macaca fascicularis	MCZ 22277	Morphosource	0.062	F	http://dx.doi.org/10.17602/M2/M3029	S1033
Macaca fascicularis	MCZ 23812	Morphosource	0.062	M	http://dx.doi.org/10.17602/M2/M3030	S1034
Macaca fascicularis	MCZ 35765	Morphosource	0.062	F	http://dx.doi.org/10.17602/M2/M3033	S1037
Macaca fascicularis	MCZ 41167	Morphosource	0.091	M	http://dx.doi.org/10.17602/M2/M3038	S1042
Mandrillus sphinx	AMNH-A 9912049	Morphosource	0.075	M	—	S5815
Mandrillus sphinx	AMNH-M 89367	Morphosource	0.080	F	urn:catalog:AMNH:Mammals:M-89367	S4599
Mandrillus sphinx	MCZ 34089	Morphosource	0.126	M	http://dx.doi.org/10.17602/M2/M5096	S1571
Mico argentatus	MCZ 30579	Morphosource	0.041	M	http://dx.doi.org/10.17602/M2/M5192	S1708
Mico argentatus	MCZ 30580	Morphosource	0.041	M	http://dx.doi.org/10.17602/M2/M5193	S1709
Mico argentatus	MCZ 32164	Morphosource	0.041	F	http://dx.doi.org/10.17602/M2/M5196	S1712
Miopithecus talapoin	MCZ 23196	Morphosource	0.050	M	http://dx.doi.org/10.17602/M2/M5094	S1665
Miopithecus talapoin	MCZ 23197	Morphosource	0.050	M	http://dx.doi.org/10.17602/M2/M5093	S1664
Miopithecus talapoin	MCZ 5547	Morphosource	0.050	M	http://dx.doi.org/10.17602/M2/M5087	S1659
Nasalis larvatus	MCZ 37341	Morphosource	0.071	F	http://dx.doi.org/10.17602/M2/M5082	S1655
Nasalis larvatus	MCZ 41560	Morphosource	0.071	F	http://dx.doi.org/10.17602/M2/M5056	S1642
Nasalis larvatus	MCZ 41562	Morphosource	0.071	F	http://dx.doi.org/10.17602/M2/M5055	S1641
Nomascus leucogenys	AMNH-M 87251	Morphosource	0.105	M	urn:catalog:AMNH:Mammals:M-87251	S5127
Pan paniscus	AMNH-M 86857	AMNH	0.116	F	urn:catalog:AMNH:Mammals:M-86857	S1590
Pan paniscus	IPS9033	CENIEH	0.066	F	—	
Pan paniscus	MCZ 38018	Morphosource	0.094	M	http://dx.doi.org/10.17602/M2/M4399	S1333

Pan paniscus	MCZ 38019	Morphosource	0.092	F	http://dx.doi.org/10.17602/M2/M4398	S1332
Pan paniscus	MCZ 38020	Morphosource	0.099	?	http://dx.doi.org/10.17602/M2/M4397	S1331
Pan troglodytes	AMNH-M 167342	Morphosource	0.089	M	urn:catalog:AMNH:Mammals:M-167342	S5129
Pan troglodytes	AMNH-M 167344	Morphosource	0.111	M	urn:catalog:AMNH:Mammals:M-167344	S5313
Pan troglodytes	IPS5698	CENIEH	0.077	M	—	
Pan troglodytes	MCZ 17702	Morphosource	0.102	F	http://dx.doi.org/10.17602/M2/M4395	S1330
Pan troglodytes	MCZ 23167	Morphosource	0.106	F	http://dx.doi.org/10.17602/M2/M4390	S1326
Pan troglodytes	MCZ 26849	Morphosource	0.106	F	http://dx.doi.org/10.17602/M2/M4388	S1324
Papio anubis	MCZ 17342	Morphosource	0.108	M	http://dx.doi.org/10.17602/M2/M4885	S1615
Papio anubis	MCZ 21160	Morphosource	0.118	M	http://dx.doi.org/10.17602/M2/M4881	S1613
Papio anubis	MCZ BOM 8304	Morphosource	0.118	M	http://dx.doi.org/10.17602/M2/M4887	S1616
Piliocolobus badius	MCZ 24080	Morphosource	0.080	M	http://dx.doi.org/10.17602/M2/M2892	S947
Piliocolobus badius	MCZ 24775	Morphosource	0.090	M	http://dx.doi.org/10.17602/M2/M2893	S948
Piliocolobus badius	MCZ 24793	Morphosource	0.080	F	http://dx.doi.org/10.17602/M2/M2894	S949
Pithecia monachus	MCZ 27124	Morphosource	0.050	?	http://dx.doi.org/10.17602/M2/M4708	S1496
Pithecia pithecia	MCZ 30718	Morphosource	0.050	M	http://dx.doi.org/10.17602/M2/M4707	S1495
Pithecia pithecia	MCZ 30719	Morphosource	0.0501	F	http://dx.doi.org/10.17602/M2/M4706	S1494
Plecturocebus cupreus	AMNH-M 72141	Morphosource	0.049	F	urn:catalog:AMNH:Mammals:M-72141	S5132
Plecturocebus cupreus	AMNH-M 72143	Morphosource	0.049	M	urn:catalog:AMNH:Mammals:M-72143	S5133
Plecturocebus cupreus	AMNH-M 75987	Morphosource	0.051	M	urn:catalog:AMNH:Mammals:M-75987	S5134
Plecturocebus cupreus	AMNH-M 75988	Morphosource	0.049	F	urn:catalog:AMNH:Mammals:M-75988	S5135
Plecturocebus cupreus	MCZ 37828	Morphosource	0.047	M	http://dx.doi.org/10.17602/M2/M5171	S1692
Pongo sp.	IPS10647	CENIEH	0.077	F	—	
Pongo sp.	IPS10651	CENIEH	0.077	F	—	
Pongo sp.	IPS9031	CENIEH	0.077	F	—	
Pongo sp.	IPSSN	CENIEH	0.077	F	—	
Pongo sp.	MCZ 37518	Morphosource	0.126	F	http://dx.doi.org/10.17602/M2/M4613	S1458

Pongo sp.	MCZ 35719	Morphosource	0.103	F	http://dx.doi.org/10.17602/M2/M4615	S1459
Presbytis rubicunda	MCZ 35704	Morphosource	0.080	F	http://dx.doi.org/10.17602/M2/M4552	S1419
Presbytis rubicunda	MCZ 35705	Morphosource	0.080	F	http://dx.doi.org/10.17602/M2/M4551	S1418
Presbytis rubicunda	MCZ 36820	Morphosource	0.080	M	http://dx.doi.org/10.17602/M2/M4554	S1420
Procolobus verus	AMNH-M 89438	Morphosource	0.076	F	urn:catalog:AMNH:Mammals:M-89438	S4627
Procolobus verus	AMNH-M 89439	Morphosource	0.080	M	urn:catalog:AMNH:Mammals:M-89439	S4628
Saguinus fuscicollis	AMNH-M 74051	Morphosource	0.027	F	urn:catalog:AMNH:Mammals:M-74051	S4404
Saguinus midas	MCZ 30597	Morphosource	0.041	M	http://dx.doi.org/10.17602/M2/M4498	S1385
Saguinus midas	MCZ 30601	Morphosource	0.041	M	http://dx.doi.org/10.17602/M2/M4497	S1384
Saimiri sciureus	MCZ 20187	Morphosource	0.047	?	http://dx.doi.org/10.17602/M2/M4486	S1373
Saimiri sciureus	MCZ 30568	Morphosource	0.047	F	http://dx.doi.org/10.17602/M2/M4483	S1370
Saimiri sciureus	MCZ 30569	Morphosource	0.047	M	http://dx.doi.org/10.17602/M2/M4447	S1362
Semnopithecus entellus	AMNH-A 9912285	Morphosource	0.060	M	—	S4396
Semnopithecus entellus	AMNH-A 9912286	Morphosource	0.108	M	—	S3764
Semnopithecus entellus	AMNH-M 90328	Morphosource	0.052	F	urn:catalog:AMNH:Mammals:M-90328	S4193
Simias concolor	AMNH-M 103369	Morphosource	0.056	M	urn:catalog:AMNH:Mammals:M-103369	S3558
Simias concolor	AMNH-M 103371	Morphosource	0.056	F	urn:catalog:AMNH:Mammals:M-103371	S3965
Symphalangus syndactylus	AMNH-M 102724	Morphosource	0.062	F	—	S5810
Symphalangus syndactylus	AMNH-M 106583	AMNH	0.079	F	urn:catalog:AMNH:Mammals:M-106583	S533
Theropithecus gelada	AMNH-M 238034	Morphosource	0.120	F	urn:catalog:AMNH:Mammals:M-238034	S4889
Theropithecus gelada	AMNH-M 60568	Morphosource	0.085	M	urn:catalog:AMNH:Mammals:M-60568	S4042
Theropithecus gelada	AMNH-M 80126	Morphosource	0.087	M	urn:catalog:AMNH:Mammals:M-80126	S4065
Trachypithecus cristatus	MCZ 35567	Morphosource	0.050	F	http://dx.doi.org/10.17602/M2/M4439	S1355
Trachypithecus cristatus	MCZ 35584	Morphosource	0.051	F	http://dx.doi.org/10.17602/M2/M4436	S1353
Trachypithecus cristatus	MCZ 35586	Morphosource	0.050	F	http://dx.doi.org/10.17602/M2/M4435	S1352

Abbreviations: F = female; M = male; ? = unknown sex; AMNH = American Museum of Natural History, New York, USA; AMNH-A = American Museum of Natural History, Anthropology Collection, New York, USA; AMNH-M = American Museum of Natural History, Mammal collection,

New York, USA; DUEA = Duke University, Evolutionary Anthropology, Durham, USA; ICP = acronym of the collections of the Institut Català de Paleontologia Miquel Crusafont, Sabadell, Spain; MCZ = Museum of Comparative Zoology, Harvard University, Cambridge, USA; MCZ-BOM = Museum of Comparative Zoology, Bones of Mammals collection, Harvard University, Cambridge, USA; SIU = Southern Illinois University, Carbondale, USA; USNM = Smithsonian National Museum of Natural History, Washington, D.C., USA.

SOM Table S2

Raw data of the variables describing the orientation, proportions and course of the carotid canal in extant anthropoid specimens.

Species	ID	2DYZA	2DXYA	$L/V^{(1/3)}$	bgPC1	bgPC2
Alouatta palliata	DUEALP 04	66.73	30.17	3.06	-0.36	0.15
Alouatta palliata	DUEALP 06	61.00	44.25	3.56	-0.40	0.17
Alouatta palliata	DUEALP 13	70.71	29.86	3.17	-0.40	0.11
Alouatta palliata	DUEALP 14	68.50	26.13	2.90	-0.34	0.09
Alouatta palliata	DUEALP 16	64.95	38.50	3.50	-0.41	0.12
Aotus griseimembra	USNM 281551	60.21	20.69	4.29	-0.41	-0.09
Aotus griseimembra	USNM 281552	57.58	16.89	3.60	-0.41	-0.13
Aotus griseimembra	USNM 284776	55.28	19.84	3.37	-0.24	-0.12
Aotus griseimembra	USNM 284777	55.09	23.71	3.90	-0.43	-0.10
Aotus griseimembra	USNM 284779	52.21	8.25	3.39	-0.27	-0.12
Ateles geoffroyi	AMNH-M 26593	59.21	32.81	3.53	-0.48	0.11
Ateles geoffroyi	MCZ 10138	50.66	38.21	3.69	-0.40	0.16
Ateles geoffroyi	MCZ 29628	57.38	39.33	4.05	-0.32	0.11
Cebus imitator	MCZ 10135	64.39	23.90	3.38	-0.41	0.02
Cebus imitator	MCZ 34326	72.30	37.16	4.01	-0.48	-0.02
Cebus imitator	MCZ 34353	64.19	26.39	4.14	-0.41	0.05
Cercocebus galeritus	AMNH-M 52641	57.39	11.66	2.40	0.24	0.04
Cercocebus torquatus	AMNH-M 70063	79.78	14.60	2.28	0.25	-0.02
Cercocebus torquatus	MCZ 32625	73.83	19.02	2.91	0.22	0.10
Cercopithecus mitis	MCZ 25022	57.20	-0.89	2.77	0.25	-0.06
Cercopithecus mitis	MCZ 26832	58.20	1.59	2.78	0.24	-0.03
Cercopithecus mitis	MCZ 7088	57.59	14.39	3.19	0.19	-0.05
Chiropotes chiropotes	USNM 388161	71.59	26.41	3.23	-0.41	0.01
Chiropotes chiropotes	USNM 388163	67.98	39.14	3.73	-0.43	0.06
Chiropotes chiropotes	USNM 388165	63.98	34.79	3.33	-0.43	0.06
Chlorocebus pygerythrus	SIU 4799	66.70	12.29	2.74	0.22	-0.10
Chlorocebus pygerythrus	SIU 4800	80.13	19.28	2.84	0.16	-0.14
Chlorocebus pygerythrus	SIU 4801	65.77	26.59	2.79	0.22	-0.02
Colobus guereza	AMNH-M 52211	71.43	26.52	2.88	0.06	0.03
Colobus guereza	AMNH-M 52213	58.93	10.06	3.13	0.10	-0.04
Colobus guereza	AMNH-M 52238	76.34	18.85	2.44	0.11	0.01
Erythrocebus patas	MCZ 47015	72.58	28.49	2.65	0.20	0.09
Erythrocebus patas	MCZ 47016	58.13	31.28	2.86	0.11	0.14

Erythrocebus patas	MCZ 47018	57.22	20.98	2.70	0.21	-0.02
Gorilla gorilla	AMNH-A 999686	56.92	10.14	3.10	0.17	0.13
Gorilla gorilla	AMNH-M 54356	50.82	6.84	2.99	0.20	0.05
Gorilla gorilla	MCZ 17684	61.71	18.12	2.85	0.19	0.17
Gorilla gorilla	MCZ 26850	55.54	3.89	3.28	0.17	0.12
Gorilla gorilla	MCZ 37264	55.97	16.40	3.24	0.18	0.07
Gorilla gorilla	MCZ 46325	56.37	12.71	3.51	0.06	0.08
Hoolock hoolock	AMNH-M 112720	52.89	4.59	2.26	0.09	-0.25
Hoolock hoolock	AMNH-M 201743	57.65	15.22	2.53	0.22	-0.10
Hoolock hoolock	AMNH-M 83425	52.54	11.33	2.57	0.22	-0.06
Hylobates agilis	IPS3773	44.51	1.00	3.19	0.20	-0.06
Hylobates lar	MCZ 41412	59.84	11.48	2.63	0.16	0.04
Hylobates lar	MCZ 41418	50.05	1.19	2.65	0.21	0.01
Hylobates lar	MCZ 41421	78.27	2.48	1.97	0.29	0.06
Hylobates lar	MCZ 41424	74.17	12.69	2.08	0.14	-0.10
Lagothrix lagotricha	USNM 269839	52.40	38.35	3.78	-0.47	0.09
Lagothrix lagotricha	USNM 461930	61.55	31.61	3.36	-0.32	0.11
Lagothrix lagotricha	USNM 545879	59.62	34.10	4.18	-0.37	0.13
Lophocebus albigena	MCZ 14725	76.19	30.79	2.53	0.06	0.00
Lophocebus albigena	MCZ 18614	69.57	7.34	3.03	0.11	-0.10
Lophocebus albigena	MCZ 22737	61.40	18.58	2.40	0.22	0.01
Macaca fascicularis	MCZ 12758	73.31	31.62	3.84	0.09	-0.06
Macaca fascicularis	MCZ 22277	70.90	13.51	2.73	0.17	-0.14
Macaca fascicularis	MCZ 23812	74.49	22.03	3.07	0.09	-0.20
Macaca fascicularis	MCZ 35765	73.79	26.47	2.21	0.25	-0.17
Macaca fascicularis	MCZ 41167	70.90	5.01	2.77	0.27	0.03
Mandrillus sphinx	AMNH-A 9912049	78.47	24.83	3.87	0.21	0.05
Mandrillus sphinx	AMNH-M 89367	69.43	13.60	2.44	0.34	-0.02
Mandrillus sphinx	MCZ 34089	70.52	2.25	2.37	0.32	0.12
Mico argentatus	MCZ 30579	79.36	33.38	4.16	-0.07	-0.14
Mico argentatus	MCZ 30580	70.89	37.76	3.40	-0.09	-0.18
Mico argentatus	MCZ 32164	71.40	36.16	3.86	-0.10	-0.16
Miopithecus talapoin	MCZ 23196	75.86	-3.12	3.74	0.10	-0.18
Miopithecus talapoin	MCZ 23197	84.14	-3.55	3.18	0.18	-0.19
Miopithecus talapoin	MCZ 5547	76.48	6.76	3.41	0.18	-0.07
Nasalis larvatus	MCZ 37341	68.96	8.49	2.94	0.17	-0.10
Nasalis larvatus	MCZ 41560	68.07	8.32	3.28	0.11	-0.12
Nasalis larvatus	MCZ 41562	69.62	2.58	2.90	0.13	-0.29

Nomascus leucogenys	AMNH-M 87251	46.95	10.01	2.88	0.32	-0.08
Pan paniscus	AMNH-M 86857	51.61	10.73	3.15	0.11	0.15
Pan paniscus	IPS9033	58.88	7.58	3.31	0.12	0.13
Pan paniscus	MCZ 38018	52.37	2.45	3.53	0.20	0.18
Pan paniscus	MCZ 38019	37.27	-0.82	3.35	0.12	0.14
Pan paniscus	MCZ 38020	44.76	10.08	3.12	0.17	0.19
Pan troglodytes	AMNH-M 167342	57.40	27.78	3.52	0.13	0.17
Pan troglodytes	AMNH-M 167344	40.91	17.19	3.42	0.08	0.13
Pan troglodytes	IPS5698	68.86	14.32	3.15	0.17	0.09
Pan troglodytes	MCZ 17702	58.80	8.02	3.44	0.13	0.13
Pan troglodytes	MCZ 23167	69.11	15.22	2.55	0.12	0.11
Pan troglodytes	MCZ 26849	65.72	19.18	3.82	0.06	0.14
Papio anubis	MCZ 17342	71.02	12.95	3.00	0.25	0.06
Papio anubis	MCZ 21160	77.92	12.01	3.06	0.23	0.04
Papio anubis	MCZ BOM 8304	84.99	13.10	2.89	0.23	0.07
Piliocolobus badius	MCZ 24080	72.37	13.36	1.80	0.23	-0.11
Piliocolobus badius	MCZ 24775	63.44	25.62	2.73	0.15	0.01
Piliocolobus badius	MCZ 24793	70.48	26.93	1.40	0.27	-0.14
Pithecia monachus	MCZ 27124	61.35	31.85	3.95	-0.35	0.09
Pithecia pithecia	MCZ 30718	65.29	33.95	4.17	-0.32	0.03
Pithecia pithecia	MCZ 30719	64.58	24.78	3.91	-0.28	0.02
Plecturocebus cupreus	AMNH-M 72141	60.37	36.47	3.82	-0.50	-0.05
Plecturocebus cupreus	AMNH-M 72143	58.98	35.27	4.03	-0.41	-0.02
Plecturocebus cupreus	AMNH-M 75987	54.55	29.05	3.95	-0.47	0.05
Plecturocebus cupreus	AMNH-M 75988	67.10	39.93	3.84	-0.45	-0.08
Plecturocebus cupreus	MCZ 37828	59.76	34.57	4.42	-0.45	0.03
Pongo sp.	IPS10647	35.58	26.47	3.08	-0.10	0.12
Pongo sp.	IPS10651	57.41	14.44	3.41	0.00	0.08
Pongo sp.	IPS9031	45.95	23.54	2.81	-0.03	0.09
Pongo sp.	IPSSN	51.04	12.11	3.22	0.19	0.20
Pongo sp.	MCZ 35719	55.71	21.61	2.61	0.14	-0.01
Pongo sp.	MCZ 37518	55.44	18.00	2.57	0.17	0.07
Presbytis rubicunda	MCZ 35704	73.37	9.72	3.28	0.05	-0.03
Presbytis rubicunda	MCZ 35705	59.19	10.94	3.26	0.07	0.02
Presbytis rubicunda	MCZ 36820	79.70	20.06	3.31	0.01	-0.05
Procolobus verus	AMNH-M 89438	72.35	13.25	3.05	0.19	-0.12
Procolobus verus	AMNH-M 89439	76.59	3.64	2.67	0.23	-0.13
Saguinus fuscicollis	AMNH-M 74051	74.69	29.71	4.08	-0.29	-0.13

Saguinus midas	MCZ 30597	79.05	43.03	3.18	-0.30	-0.26
Saguinus midas	MCZ 30601	75.43	34.46	3.27	-0.22	-0.17
Saimiri sciureus	MCZ 20187	68.68	38.36	2.91	-0.49	-0.09
Saimiri sciureus	MCZ 30568	67.23	27.31	3.44	-0.36	-0.09
Saimiri sciureus	MCZ 30569	70.14	38.60	3.48	-0.37	-0.10
Semnopithecus entellus	AMNH-A 9912285	66.06	28.37	2.52	0.12	0.05
Semnopithecus entellus	AMNH-A 9912286	64.95	33.39	3.01	0.16	0.05
Semnopithecus entellus	AMNH-M 90328	62.09	25.82	3.17	0.12	0.01
Simias concolor	AMNH-M 103369	73.52	29.07	3.13	0.08	-0.12
Simias concolor	AMNH-M 103371	71.86	33.87	3.40	-0.11	-0.10
Symphalangus syndactylus	AMNH-M 102724	38.27	19.77	3.37	0.08	0.12
Symphalangus syndactylus	AMNH-M 106583	44.54	23.27	3.32	0.06	0.00
Theropithecus gelada	AMNH-M 238034	66.58	7.26	2.87	0.28	0.05
Theropithecus gelada	AMNH-M 60568	68.61	20.77	3.02	0.27	0.06
Theropithecus gelada	AMNH-M 80126	65.87	24.69	3.11	0.21	0.08
Trachypithecus cristatus	MCZ 35567	58.10	27.71	3.38	0.13	-0.07
Trachypithecus cristatus	MCZ 35584	80.20	17.07	3.23	0.26	-0.12
Trachypithecus cristatus	MCZ 35586	61.67	21.44	3.35	0.22	-0.02

Abbreviations: 2DYZA = 2D angle in the YZ plane (canal superior orientation; in degrees); 2DXYA = 2D angle in the XY plane (canal medial orientation; in degrees); L = length (in mm); V = volume (in mm^3); bgPC = between-group principal component; AMNH = American Museum of Natural History, New York, USA; AMNH-A = American Museum of Natural History, Anthropology Collection, New York, USA; AMNH-M = American Museum of Natural History, Mammal collection, New York, USA; DUEA = Duke University, Evolutionary Anthropology, Durham, USA; ICP = acronym of the collections of the Institut Català de Paleontologia Miquel Crusafont, Sabadell, Spain; MCZ = Museum of Comparative Zoology, Harvard University, Cambridge, USA; MCZ-BOM = Museum of Comparative Zoology, Bones of Mammals collection, Harvard University, Cambridge, USA; SIU = Southern Illinois University, Carbondale, USA; USNM = Smithsonian National Museum of Natural History, Washington, D.C., USA.

SOM Table S3

Results of the Kruskal-Wallis comparisons for the indices and bgPCs describing the orientation, proportions and course of the carotid canal in the main extant anthropoid clades.

	H	*p*
2DYZA	45.74	<0.001
2DXYA	58.57	<0.001
$L/V^{(1/3)}$	63.73	<0.001
bgPC1	83.36	<0.001
bgPC2	39.31	<0.001

Abbreviations: 2DYZA = 2D angle in the YZ plane (canal superior orientation; in degrees); 2DXYA = 2D angle in the XY plane (canal medial orientation; in degrees); L = length (in mm); V = volume (in mm^3); bgPC = between-group principal component; H = Kruskal-Wallis statistic.

SOM Table S4

Results of the Bonferroni-corrected Mann-Whitney post hoc pairwise comparisons for the indices and bgPCs describing the orientation, proportions and course of the carotid canal in the main extant anthropoid clades.

	Platyrrhini	Cercopithecidae	Hominidae	Hylobatidae
2DYZA				
Platyrrhini	—	<0.01	<0.001	0.035
Cercopithecidae	<0.01	—	<0.001	<0.01
Hominidae	<0.001	<0.001	—	1
Hylobatidae	0.035	<0.01	1	—
2DXYA				
Platyrrhini	—	<0.001	<0.001	<0.001
Cercopithecidae	<0.001	—	1	0.240
Hominidae	<0.001	1	—	1
Hylobatidae	<0.001	0.240	1	—
$L/V^{(1/3)}$				
Platyrrhini	—	<0.001	<0.001	<0.001
Cercopithecidae	<0.001	—	<0.01	1
Hominidae	<0.001	<0.01	—	0.016
Hylobatidae	<0.001	1	0.016	—
bgPC1				
Platyrrhini	—	<0.001	<0.001	<0.001
Cercopithecidae	<0.001	—	0.068	1
Hominidae	<0.001	0.068	—	0.390
Hylobatidae	<0.001	1	0.390	—
bgPC2				
Platyrrhini	—	0.760	<0.001	1
Cercopithecidae	0.760	—	<0.001	1
Hominidae	<0.001	<0.001	—	<0.001
Hylobatidae	1	1	<0.001	—

Abbreviations: 2DYZA = 2D angle in the YZ plane (canal superior orientation; in degrees); 2DXYA = 2D angle in the XY plane (canal medial orientation; in degrees); L = length (in mm); V = volume (in mm^3); bgPC = between-group principal component.

SOM Table S5

Results of the permutational analysis of variance based on the Euclidean distances between group means. Groups correspond to the main extant anthropoid clades (i.e., platyrrhines, cercopithecids, hylobatids, and hominids) used in the bgPCA and further analyses (see the main text). The tests have been computed with the streampoint configurations (i.e., full space) and with the bgPC scores with and without cross-validation (i.e., bgPCA spaces). While *p* is the significance of group mean differences, the coefficient of determination (R^2) denotes the variance explained by the grouping structure.

	p	R^2
Full space	0.001	0.67
bgPCA space without CV	0.001	0.77
bgPCA space with CV	0.001	0.77

Abbreviations: bgPCA = between-group principal component analysis; CV = cross-validation.

SOM File S1. R script used to import the 3D carotid canal surface and iteratively find the orthogonal plane to the canal passing through IRG (intersection ridge–groove) among several cutting plane possibilities. (Provided as a separate R file.)

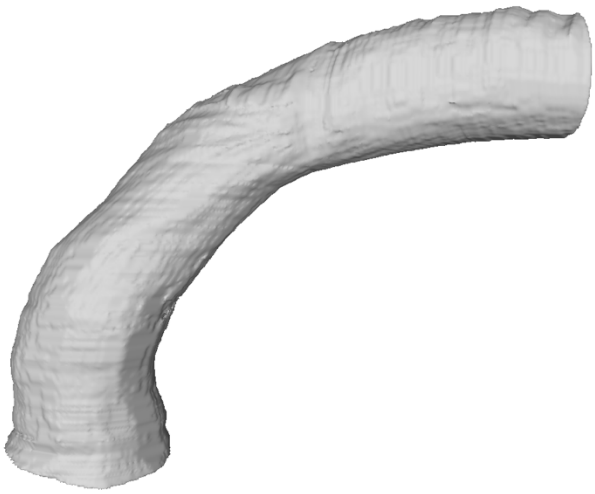

SOM File S2. 3D model of the carotid canal surface of *Pliobates cataloniae*, available from MorphoSource.org (http://dx.doi.org/10.17602/M2/M344218).

SOM References

Adams, D.C., Collyer, M.L., Kaliontzopoulou, A., 2019. Geomorph: Software for geometric morphometric analyses. R Package Version 3.3.1. https://cran.r-project.org/web/packages/geomorph/index.html.

Alba, D.M., Almécija, S., DeMiguel, D., Fortuny, J., Pérez de los Ríos, M., Pina, M., Robles, J.M., Moyà-Solà, S., 2015. Miocene small-bodied ape from Eurasia sheds light on hominoid evolution. Science 350, aab2625.

Alba, D.M., Casanovas-Vilar, I., Garcés, M., Robles, J.M., 2017. Ten years in the dump: An updated review of the Miocene primate-bearing localities from Abocador de Can Mata (NE Iberian Peninsula). J. Hum. Evol. 102, 12–20.

Arnold, C., Matthews, L.J., Nunn, C.L., 2010. The 10kTrees website: A new online resource for primate phylogeny. Evol. Anthropol. 19, 114–118.

Begun, D.R., 2017. Evolution of the Pliopithecoidea. In: Fuentes, A. (Ed.), The International Encyclopedia of Primatology. John Wiley & Sons, Hoboken. https://doi.org/10.1002/9781119179313.wbprim0165.

Benefit, B.R., 1999. *Victoriapithecus*: The key to Old World monkey and catarrhine origins. Evol. Anthropol. 7, 155–174.

Bookstein, F.L., 1991. Morphometric Tools for Landmark Data: Geometry and Biology. Cambridge University Press, Cambridge.

Drake, R.E., Van Couvering, J.A., Pickford, M.H., Curtis, G.H., Harris, J.A., 1988. New chronology for the Early Miocene mammalian faunas of Kisingiri, Western Kenya. J. Geol. Soc. 145, 479–491.

Gilbert, C.C., Ortiz, A., Pugh, K.D., Campisano, C.J., Patel, B.A., Premjit, N., Fleagle, J.G., Patnaik, R., 2020. New Middle Miocene ape (Primates: Hylobatidae) from Ramnagar, India fills major gaps in the hominoid fossil record. Proc. R. Soc. B. 287, 20201655.

Harrison, T., 2010. Dendropithecoidea, Proconsuloidea and Hominoidea (Catarrhini, Primates). In: Werdelin, L., Sanders, W.J. (Eds.), Cenozoic Mammals of Africa. University of California Press, Berkeley, pp. 429–469.

Harrison, T., 2013. Catarrhine origins. In: Begun, D.R. (Ed.), A Companion to Paleoanthropology. Blackwell Publishing, Oxford, pp. 376–396.

Harrison, T., 2017. Miocene primates. In: Fuentes, A. (Ed.), The International Encyclopedia of Primatology. John Wiley & Sons, Hoboken. https://doi.org/10.1002/9781119179313.wbprim0227.

Meyer, D., Rinaldi, Ir.D., Ramlee, H., Perwitasari-Farajallah, D., Hodges, J.K., Roos, C., 2011. Mitochondrial phylogeny of leaf monkeys (genus *Presbytis*, Eschscholtz, 1821) with implications for taxonomy and conservation. Mol. Phylogenet. Evol. 59, 311–319.

Nengo, I., Tafforeau, P., Gilbert, C.C., Fleagle, J.G., Miller, E.R., Feibel, C., Fox, D.L., Feinberg, J., Pugh, K.D., Berruyer, C., Mana, S., Engle, Z., Spoor, F., 2017. New infant cranium from the African Miocene sheds light on ape evolution. Nature 548, 169–174.

R Core Team, 2020. R: A language and environment for statistical computing. R Foundation for Statistical Computing, Vienna.

Peppe, D.J., McNulty, K.P., Cote, S.M., Harcourt-Smith, W.E.H., Dunsworth, H.M., VanCouvering, J.A., 2009. Stratigraphic interpretation of the Kulu Formation (Early Miocene, Rusinga Island, Kenya) and its implications for primate evolution. J. Hum. Evol. 56, 447–461.

Rohlf, F.J., Slice, D.E., 1990. Extensions of the Procrustes method for the optimal superimposition of landmarks. Syst. Zool. 39, 40–59.

Spoor, F. 1993. The comparative morphology and phylogeny of the human bony labyrinth. Ph.D. Dissertation, Utrecht University.

Springer, M.S., Meredith, R.W., Gatesy, J., Emerling, C.A., Park, J., Rabosky, D.L., Stadler, T., Steiner, C., Ryder, O.A., Janečka, J.E., Fisher, C.A., Murphy, W.J., 2012. Macroevolutionary dynamics and historical biogeography of primate diversification inferred from a species supermatrix. PLoS One 7, e49521.

Urciuoli, A., Zanolli, C., Beaudet, A., Dumoncel, J., Santos, F., Moyà-Solà, S., Alba, D.M., 2020. The evolution of the vestibular apparatus in apes and humans. eLife 9, e51261.

van der Meulen, A.J., García-Paredes, I., Álvarez-Sierra, M.Á., van den Hoek Ostende, L.W., Hordijk, K., Oliver, A., López-Guerrero, P., Hernández-Ballarín, V., Peláez-Campomanes, P., 2011. Biostratigraphy or biochronology? Lessons from the Early and Middle Miocene small Mammal Events in Europe. Geobios 44, 309–321.